

Block Magnetic Excitations in the Orbitorally Selective Mott Insulator BaFe₂Se₃

M. Mourigal,^{1,*} Shan Wu,¹ M. B. Stone,² J. R. Neilson,^{1,3,†} J. M. Caron,^{1,3} T. M. McQueen,^{1,3,4} and C. L. Broholm^{1,2,4}

¹*Institute for Quantum Matter and Department of Physics and Astronomy,*

Johns Hopkins University, Baltimore, Maryland 21218, USA

²*Quantum Condensed Matter Division, Oak Ridge National Laboratory, Oak Ridge, Tennessee 37831, USA*

³*Department of Chemistry, Johns Hopkins University, Baltimore, Maryland 21218, USA*

⁴*Department of Materials Science and Engineering, Johns Hopkins University, Baltimore, Maryland 21218, USA*

(Received 12 November 2014; published 23 July 2015)

Iron pnictides and selenides display a variety of unusual magnetic phases originating from the interplay between electronic, orbital, and lattice degrees of freedom. Using powder inelastic neutron scattering on the two-leg ladder BaFe₂Se₃, we fully characterize the static and dynamic spin correlations associated with the Fe₄ block state, an exotic magnetic ground state observed in this low-dimensional magnet and in Rb_{0.89}Fe_{1.58}Se₂. All the magnetic excitations of the Fe₄ block state predicted by an effective Heisenberg model with localized spins are observed below 300 meV and quantitatively reproduced. However, the data only account for 16(3) μ_B^2 per Fe²⁺, approximately 2/3 of the total spectral weight expected for localized $S = 2$ moments. Our results highlight how orbital degrees of freedom in iron-based magnets can conspire to stabilize an exotic magnetic state.

DOI: 10.1103/PhysRevLett.115.047401

PACS numbers: 78.70.Nx, 74.70.Xa, 75.10.Pq, 75.30.Ds

Magnetism in iron-based superconductors is a complex many-body phenomenon, and understanding it is now a central challenge in condensed-matter physics [1,2]. The parent compounds of a large majority of iron-based superconductors are constructed from quasi-two-dimensional (2D) FeAs or FeSe layers and host a range of metallic, semimetallic, and insulating behaviors originating from the interplay between structural, orbital, magnetic, and electronic degrees of freedom [3–6]. Their magnetic ground states and excitations have been extensively studied by neutron scattering [7–12], but a unified theoretical description that accounts for the role of Coulomb repulsion and Hund’s coupling on electrons occupying multiple active 3*d* orbitals remains a challenging task. To understand these unfamiliar Fe-based magnets it is necessary to probe electronic correlations at the atomic scale in chemically and structurally related materials.

Inspired by the successful description of magnetic, electronic, and orbital phenomena in various insulating chain- and ladder-based cuprates [13–15], recent experimental work explored the properties of structurally quasi-one-dimensional (1D) Fe-based compounds such as KFe₂Se₃ [16], CsFe₂Se₃ [17], BaFe₂Se₂O [18], TaFe_{1+y}Te₃ [19], and the two-leg ladder BaFe₂Se₃ [20–25]. Unlike the former materials, BaFe₂Se₃ hosts an exotic form of magnetic order, the Fe₄ block state, that has also been observed in the $\sqrt{5} \times \sqrt{5}$ vacancy-ordered quasi-2D compound Rb_{0.89}Fe_{1.58}Se₂ [11,26] and reproduced by first-principles electronic structure calculations [27]. Facilitated by low dimensionality, exact diagonalization (ED) and density-matrix renormalization group (DMRG) analysis [28,29] of multiorbital Hubbard models relevant for BaFe₂Se₃ indicate the exotic block

state is stabilized by sizable Hund’s coupling [28,29]. It is proposed that BaFe₂Se₃ forms an *orbital-selective Mott phase* [29] where narrow-band localized electrons coexist with wideband itinerant electrons originating from different 3*d* atomic orbitals [27,30].

In this work, we determine the magnetic excitation spectrum of BaFe₂Se₃ through broadband inelastic neutron scattering from a powder sample. We provide direct spectroscopic evidence for the Fe₄ block state (Fig. 1) and develop an effective Heisenberg model that accounts for all observed acoustic and optical spin-wave modes. We also determine the effective moment in the energy range below 300 meV to be $\mu_{\text{eff}}^2 \approx 16\mu_B^2$ per Fe, which is indicative of spin-orbital magnetism in BaFe₂Se₃.

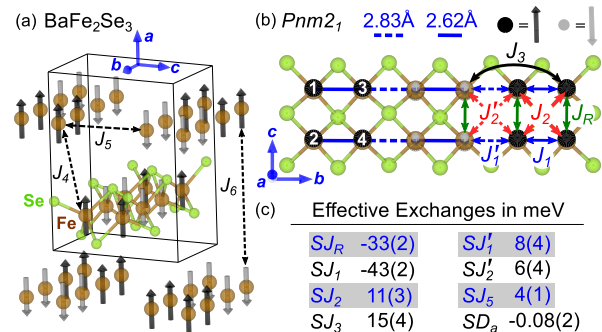


FIG. 1 (color online). (a) Crystal structure of BaFe₂Se₃ with $a = 11.88$ Å, $b = 5.41$ Å, and $c = 9.14$ Å. Ba atoms are omitted. The Fe₄ block ground state is represented with light (spin-down) and dark (spin-up) bold arrows. (b) Structure of an individual ladder. (c) Values of exchange interactions determined from our data using an effective Heisenberg model.

The crystal structure of BaFe_2Se_3 (Fig. 1) determined by low-temperature neutron powder diffraction (NPD) [20,21,23,31] comprises edge-sharing FeSe_4 tetrahedra forming two-leg Fe ladders organized in a face-centered orthorhombic lattice. Neutron pair-distribution-function (NPDF) analysis [16,20] reveals gradual Fe displacements upon cooling leading to *structural* Fe_4 blocks (plaquettes) [Fig. 1(b)] with two inequivalent Fe sites in the $Pnm2_1$ space group. The Fe environments are distorted with four distinct distances to coordinating Se atoms. BaFe_2Se_3 is an insulator with a resistivity activation energy of $E_a \approx 0.13\text{--}0.18$ eV [21,23]. Assuming a high-spin electronic configuration in the tetrahedral crystal field leads to $S = 2$ per $\text{Fe}^{2+} 3d^6$ ions. Long-range magnetic order develops below $T_N \approx 255$ K with a saturated moment of $2.8\mu_B$ per Fe [20,21] and a propagation vector $\kappa = (\frac{1}{2}, \frac{1}{2}, \frac{1}{2})$. The corresponding magnetic structure consists of Fe_4 blocks in which four nearest-neighbor spins coalign parallel to the a direction [20,21]. In turn, the plaquettes arrange in a staggered fashion along the ladder and interladder directions [Fig. 1(a)] with no net magnetization. This exotic magnetic state points to exchange frustration, orbital ordering, and/or spin-lattice coupling, and it was recently proposed that BaFe_2Se_3 may host a ferroelectric polarization driven by exchange striction [32].

To search for magnetic excitations associated with the Fe_4 block spin structure, our inelastic neutron scattering experiment was performed on the ARCS [33] time-of-flight spectrometer at the Spallation Neutron Source (SNS), Oak Ridge National Laboratory (ORNL). A $m \approx 9.9$ g power sample of BaFe_2Se_3 , synthesized using the method of Ref. [20], was mounted in a cylindrical aluminum can, sealed under 1 atm of ^4He , and cooled to $T = 5$ K in a close-cycle cryostat. To reduce multiple scattering, the can contained horizontal sheets of neutron absorbing Cd inserted every centimeter between layers of BaFe_2Se_3 powder. Data were acquired with the incident neutron energy set to $E_i = 20, 50, 150,$ and 450 meV with full width at half maximum (FWHM) elastic energy resolution of 0.8, 2.0, 5.8, and 40 meV, respectively, and momentum resolution of 0.060(4), 0.079(6), 0.11(1), and 0.20(3) \AA^{-1} estimated from the average FWHM of the four strongest nuclear reflections below $Q \leq 2.2$ \AA^{-1} . The intensity measured as a function of momentum $\hbar Q = \hbar|\mathbf{Q}|$ and energy transfer $E = \hbar\omega$, $\tilde{I}(Q, E) = k_i/k_f(d^2\sigma/d\Omega dE_f)$, was normalized to absolute units ($\text{mbarn sr}^{-1} \text{meV}^{-1} \text{Fe}^{-1}$) using the integrated intensity of nuclear Bragg scattering in the paramagnetic phase at $T = 300$ K. This method was preferred over normalization to a vanadium standard to ensure a reliable cross calibration between data sets with very different E_i .

In Fig. 2, we discuss the elastic scattering and spectrum of low-energy excitations measured in BaFe_2Se_3 . At $T = 5$ K [Fig. 2(a)], we observe an intense ridge of inelastic signal which extends from $E \approx 4$ meV and is characterized by a sharp onset at $Q \approx 0.7$ \AA^{-1} and a more gradual decay towards larger Q . A similar asymmetric line shape is

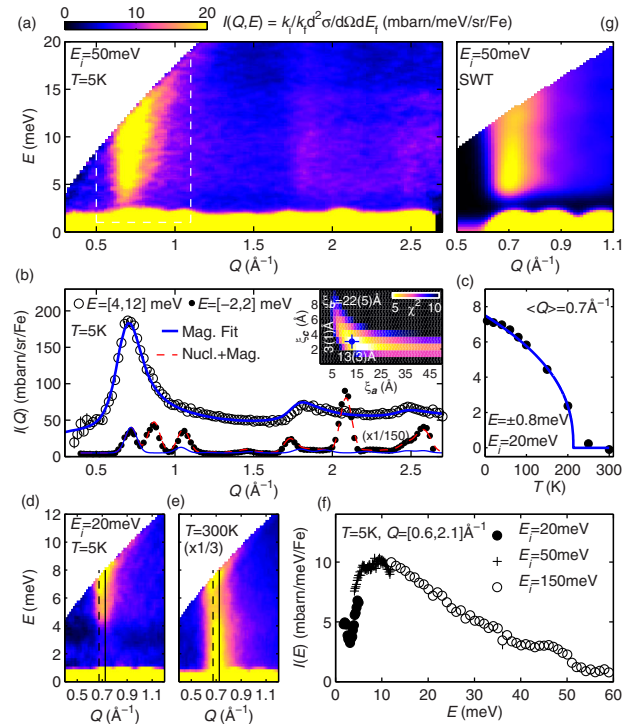


FIG. 2 (color online). Low-energy spectrum of BaFe_2Se_3 . (a) $\tilde{I}(Q, E)$ at $T = 5$ K with $E_i = 50$ meV. (b) E -integrated inelastic scattering $\tilde{I}(Q)$ (open symbols) and elastic scattering $\tilde{I}_0(Q)$ multiplied by a factor 1/150 (full symbols) compared to the text's model cross section (solid blue line) and elastic scattering (dashed red line). Inset: Fit χ^2 versus ξ_a and ξ_c and best fit values (blue symbol). (c) T dependence of the integrated magnetic intensity measured with $E_i = 20$ meV (full symbols) and magnetic order parameter as a guide to the eye (blue line). (d,e) $\tilde{I}(Q, E)$ with $E_i = 20$ meV at $T = 5$ K and $T = 300$ K. (f) Momentum-integrated inelastic scattering with different E_i 's. (g) SWT prediction $\tilde{I}_{\text{SWT}}(Q, E)$ for $E_i = 50$ meV in arbitrary intensity units.

observed for $Q \approx 1.8$ and 2.5 \AA^{-1} . The corresponding $\tilde{I}(Q)$ obtained by E integration over the range $4 \leq E \leq 12$ meV is compared to the scaled elastic signal $\tilde{I}_0(Q)$ integrated over $E = \pm 2$ meV in Fig. 2(b). The coherent elastic signal can be reproduced without any free parameter using the known magnetic propagation vector κ , Fe_4 block spin structure, and a static moment of $\langle m \rangle = 2.7(1)\mu_B$ per Fe. The latter value is extracted from the low-temperature limit for $|E| < 0.8$ meV [Fig. 2(c)], corresponds to a static spin value $\langle S \rangle = 1.3(1)$ for $g = 2$, and agrees remarkably well with the value obtained by neutron diffraction [16,20,21]. As maxima in $\tilde{I}(Q)$ are observed around strong magnetic Bragg reflections of $\tilde{I}_0(Q)$, the former signal clearly originates from acoustic spin waves and contains information particularly about interplaquette magnetic interactions in BaFe_2Se_3 .

To determine the dimensionality of magnetism in BaFe_2Se_3 , we use an approach employed for spatially short-range ordered states [34,35] and compare the

E -integrated inelastic signal to the spherical average of the orthorhombic scattering cross section

$$\tilde{I}(Q) \propto \int \frac{d\Omega}{4\pi} |f(\mathbf{Q})|^2 \sum_{\tau_m} \frac{|\mathbf{F}_{\perp}(\boldsymbol{\tau}_m)|^2}{(1 + \sum_{\alpha=1}^3 \xi_{\alpha}^2 [(\mathbf{Q} - \boldsymbol{\tau}_m) \cdot \hat{\mathbf{e}}_{\alpha}]^2)^2},$$

where $f(\mathbf{Q})$ is the magnetic form factor of Fe^{2+} , $\mathbf{F}_{\perp}(\mathbf{Q})$ is the magnetic scattering amplitude perpendicular to the momentum transfer \mathbf{Q} , and $\boldsymbol{\tau}_m = \boldsymbol{\tau} \pm \boldsymbol{\kappa}$ with $\boldsymbol{\tau} = h\mathbf{a}^* + k\mathbf{b}^* + \ell\mathbf{c}^*$ a reciprocal-lattice vector. The parameters ξ_{α} with $\alpha = 1, 2, 3$ are pseudocorrelation lengths along the crystallographic directions \mathbf{a} , \mathbf{b} , and \mathbf{c} , respectively. A fit to the asymmetric inelastic profile for $Q \leq 2.8 \text{ \AA}^{-1}$ [Fig. 2(b)], for which the Ewald sphere passes through ≈ 200 magnetic peaks at distinct angles, robustly identifies anisotropic correlation lengths $\xi_a = 3(1) \text{ \AA}$, $\xi_b = 22(5) \text{ \AA}$, and $\xi_c = 13(3) \text{ \AA}$ [inset of Fig. 2(b)]. In terms of interplaquette distances in the orthorhombic unit cell (Fig. 1), these correspond to $\xi_b = 4.1(8)\mathbf{b}$, $\xi_c = 1.4(3)\mathbf{c}$, and $\xi_a = 0.3(1)\mathbf{a}$. Qualitatively, this reveals that BaFe_2Se_3 is a low-dimensional magnet with a hierarchy of interactions that result in zero-dimensional Fe_4 blocks arranged as quasi-one-dimensional ladders extending along \mathbf{b} that in turn interact weakly with their nearest neighbors to form a quasi-two-dimensional spin system in the bc plane.

Our higher-resolution $E_i = 20 \text{ meV}$ data reveal an apparent gap $\Delta \approx 5 \text{ meV}$ in the spectrum for $T = 5 \text{ K}$ [Fig. 2(d)]. While this gap closes when warming to $T = 300 \text{ K}$, the Δ energy scale remains apparent. The signal's line shape changes from a Gaussian peak centered at $Q \approx 0.72 \text{ \AA}^{-1} = |\boldsymbol{\kappa}|$ for $E < \Delta$ to an asymmetric peak shape that onsets at $Q \approx 0.68 \text{ \AA}^{-1} = |(0, \frac{1}{2}, \frac{1}{2})|$ for $E > \Delta$, where it resembles the line shape of the low-temperature spectrum. This behavior can be qualitatively understood as a consequence of the dimensionality of the interladder interactions and a small single ion or exchange anisotropy responsible for Δ .

To determine the bandwidth of the acoustic spin waves in BaFe_2Se_3 , we turn to the E dependence of the low-energy signal $\tilde{I}(E)$ integrated over $0.6 \leq Q \leq 2.1 \text{ \AA}^{-1}$ with $E_i = 150 \text{ meV}$ [Fig. 2(f)]. The low-energy excitations extend continuously from $E \approx \Delta$ up to $E \approx 50 \text{ meV}$, with a small peak at $E_1 = 46(1) \text{ meV}$ indicating the top of the acoustic spin-wave band [see also Fig. 3(c)]. As we shall see, this conventional 45 meV wide spectrum of acoustic spin waves belies the exotic Fe_4 block state.

It is the higher-energy excitations of BaFe_2Se_3 (Fig. 3) that offer salient signatures of Fe_4 block magnetic order. With $E_i = 450 \text{ meV}$ [Fig. 3(a)] and $E_i = 150 \text{ meV}$ [Fig. 3(b)], the experiment covers a large dynamical range and reveals three additional bands of excitations, labeled $n = 2, 3$, and 4 in the following. Two of these are centered around $E \approx 100 \text{ meV}$ with $E_2 = 88.9(1) \text{ meV}$ and $E_3 = 108.2(5) \text{ meV}$, and the highest-energy excitation is found at $E_4 = 198(1) \text{ meV}$ [Fig. 3(c)]. Their corresponding widths

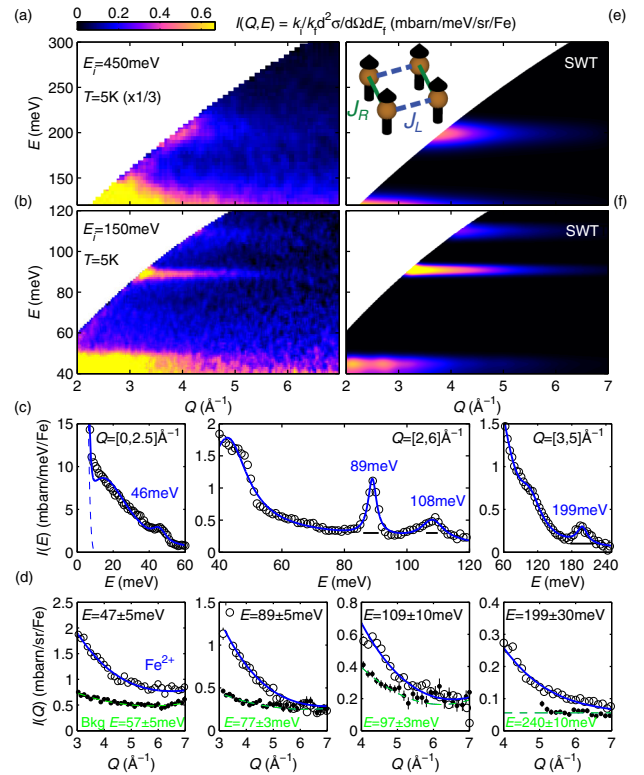


FIG. 3 (color online). High-energy spectrum of BaFe_2Se_3 . (a), (b) Intensity plot of $\tilde{I}(Q, E)$ at $T = 5 \text{ K}$ with (a) $E_i = 450 \text{ meV}$ and (b) $E_i = 150 \text{ meV}$. (c) Momentum-integrated inelastic scattering $\tilde{I}(E)$ (open symbols) for various ranges of Q and fits to Lorentzian line shapes (solid blue lines). (d) Energy-integrated inelastic scattering $\tilde{I}(Q)$ for the four modes (open symbols) compared to the nearby background $B(Q)$ (full symbols) and to the Fe^{2+} form factor $I(Q) = A|f(Q)|^2 + B(Q)$ (solid blue lines). (e), (f) SWT prediction $I_{\text{SWT}}(Q, E)$ for (e) $E_i = 450 \text{ meV}$ and (f) $E_i = 150 \text{ meV}$ in arbitrary units.

(Lorentzian FWHM) $\Gamma_n = 1.7(2)$, $4(1)$, and $15(3) \text{ meV}$, respectively, can be compared with a geometry-based calculation of the energy resolution of the spectrometer at $E = E_n$, $\delta E_n = 2.2(4)$, $1.8(4)$, and $18(4) \text{ meV}$, respectively. Although these overestimate the resolution width by 20%, they indicate the $n = 2$ and $n = 4$ modes are close to being resolution limited while the $n = 3$ excitation is intrinsically broad. The Q dependence of all four bands of magnetic excitations [Fig. 3(d)] compare well with the Fe^{2+} form factor for $Q \geq 3\text{--}4 \text{ \AA}^{-1}$, $\tilde{I}(Q) \propto |f(Q)|^2$, and contrasts with the approximately Q -independent background. Given the form factor and the fact that charge and intraorbital dd excitations (crystal-field excitations) have been observed by resonant inelastic x-ray scattering (RIXS) [25] at higher energies $E \approx 0.35 \text{ eV}$ and $E \approx 0.65 \text{ eV}$, respectively, we infer the signal arises from intra- Fe_4 block excitations (optical spin waves).

We can then extract the (total) dynamical spin correlation function for each band of scattering $g^2 \tilde{S}_n(Q, E) = 6\tilde{I}_n(Q, E)/|r_0 f(Q)|^2$ with $r_0 = 0.539 \times 10^{-12} \text{ cm}$ and subsequently obtain the inelastic spectral weight per Fe and

TABLE I. Integrated elastic intensity $\langle m \rangle^2$ and inelastic spectral weight δm_n^2 per spin-wave mode at $T = 5$ K. The error bars correspond to statistical uncertainty and do not include systematic errors in the normalization and background subtraction procedures estimated at 20%.

Spectral weight	$\langle m \rangle^2$	δm_1^2	δm_2^2	δm_3^2	δm_4^2	m_{tot}^2
$\mu_B^2 \cdot \text{Fe}^{-1}$	7.5(3)	5.8(1)	0.5(1)	0.9(1)	1.0(1)	15.7(2)

per mode $\delta m_n^2 = \mu_B^2 \int \int Q^2 [g^2 \tilde{S}_n(Q, E)] dQ dE / \int Q^2 dQ$. After background subtraction and adapting the integration range to the bandwidth of each mode, we obtain Table I. Summing the observed static $\langle m \rangle^2$ and dynamic δm^2 spin correlations yields a total spectral weight of $m_{\text{tot}}^2 = 16(3)\mu_B^2$ per Fe. This is significantly smaller than $g^2 S(S+1)\mu_B^2 = 24\mu_B^2$ expected for $g = 2$ and $S = 2$. The total inelastic contribution of $8.2(2)\mu_B^2$ per Fe is, however, larger than $g^2 \langle S \rangle \mu_B^2 = 5.2(4)\mu_B^2$ which indicates an unusual magnetic ground state in BaFe_2Se_3 with a reduced ordered moment and enhanced spin fluctuations. Remarkably, the total moment that we detect is consistent with the prediction of $16\mu_B^2$ per Fe obtained for the Fe_4 block in Ref. [28] from a Hartree-Fock treatment of a five-band Hubbard model.

We now develop an effective spin- S Heisenberg model for BaFe_2Se_3 . We start from an isolated rectangular Fe_4 block with ferromagnetic J_R and J_L exchange interactions along its rungs and legs, respectively [inset of Fig. 3(e)]. An elementary diagonalization yields four localized excitations at energies $\tilde{\epsilon}_n = 0, 2SJ_L, 2SJ_R$, and $2S(J_R + J_L)$. These resemble our observations of high-energy optical spin waves with the ferromagnetic exchange parameters $SJ_L \approx -44$ meV and $SJ_R \approx -54$ meV or their permutation. The long-range ordered state, the wide acoustic band, and the broadened 108 meV mode imply intraladder and interladder exchange interactions that we parametrize consistent with the $Pnm2_1$ structure and the effects of which we describe with linear spin-wave theory (SWT) [Fig. 1(b)]. These interactions can originate from Fe-Se-Fe and Fe-Se-Se-Fe superexchange paths or from electronic ring-exchange terms that are indistinguishable from further-neighbor exchange at the level of linear SWT [36].

Considering an isolated single ladder with Fe_4 block spin structure, linear SWT yields four spin-wave modes ϵ_n that directly stem from the above localized modes $\tilde{\epsilon}_n$. Their energies are $\epsilon_n(k) = S\sqrt{A_n^2 - B_n^2 \cos(4\pi k)}/\sqrt{2}$ where A_n determines the average energy of each mode and $B_n = (\pm J'_1 \pm J'_2 \pm 2J_3)$ controls the bandwidth of their dispersion, with sign combinations $(+++)$, $(+-+)$, $(++-)$, and $(-++)$ for $n = 1, 2, 3$, and 4, respectively. The constant A_n depends on $J_R, J_1, J'_1, J_2, J'_2$, and J_3 . As for the isolated Fe_4 block, J_R and J_1 ($\equiv J_L$) control the overall energy scale and the splitting between ϵ_2 and ϵ_3 . As the lowest-energy mode acquires a bandwidth controlled by $J'_1 + J'_2 + 2J_3$, we expect reduced values for J_R and J_1 compared to an isolated plaquette. We also

anticipate a sizable J_2 to account for the relative position of ϵ_2 and ϵ_3 with respect to ϵ_4 . As J'_1 and J'_2 constrain the bandwidth of the high-energy modes, their values are important to allow a broad ϵ_3 while keeping the widths of ϵ_2 and ϵ_4 limited to the resolution of the instrument.

To obtain realistic values for these exchanges, we compared the experimental energies $E_{n=1,2,3,4}$ and intrinsic widths $\Gamma_{n=2,3,4}$ to predictions from the analytical SWT model convoluted with the estimated instrumental resolution. A least-squares fit to the above seven experimental constraints yields $SJ_R = -43(2)$ meV, $SJ_1 = -33(2)$ meV, $SJ'_1 = 8(4)$ meV, $SJ_2 = 11(3)$ meV, $SJ'_2 = 6(4)$ meV, and $SJ_3 = 15(4)$ meV; see also Figs. 1(b) and 1(c). Our model includes a small easy a -axis anisotropy $|SD_a| = 0.08(2)$ meV to account for the spin gap. In addition, the steep spin-wave dispersion and the absence of enhanced density of states (typically associated with interchain coupling) below 20 meV [Fig. 2(a)] indicate interladder exchanges greater than 3 meV. The latter is included in the above model through $SJ_5 = 4(1)$ meV, but the data can be described without J_4 and J_6 [Fig. 1(a)]. Using the numerical implementation of linear SWT [37,38] in the SPINW program [38], the powder averaged scattering intensity $I_{\text{SWT}}(Q, E)$ for the model and exchanges of Figs. 1(b) and 1(c) is shown in Figs. 2(g), 3(e), and 3(f). The model accounts for all significant aspects of the data [Figs. 2(a), 3(a), and 3(b)], and, in turn, the data provide evidence for all the magnetic excitations expected for the Fe_4 block state.

We have shown that BaFe_2Se_3 is a nearly spin-isotropic low-dimensional antiferromagnet with a sizable ratio between interladder and intraladder interactions $4J_5/(J'_1 + J'_2 + 2J_3) \approx 0.45$. We have determined a set of exchange interactions, compatible with the $Pnm2_1$ structure, that stabilizes the Fe_4 block ground state and produces the peculiar multiband excitation spectrum that we detected. Our experiment recovers a large fraction of, but not the entire, spectral weight expected for localized Fe moments. Large missing neutron intensity was previously reported in insulating cuprates such as the spin-chain compound Sr_2CuO_3 [39] and attributed to hybridization between the magnetic Cu- $3d$ orbital and O- $2p$ orbitals. While our experiment cannot directly probe hybridization effects between the magnetic Fe- $3d$ and Se- $4p$ orbitals, the reduced effective moment observed in BaFe_2Se_3 is remarkably consistent with the predictions for an orbital-selective Mott state [16,29]. This strongly favors a scenario where only $\approx 2/3$ of the $3d$ electrons of Fe participate in the formation of local moments while the remaining electrons occupy wide electronic bands and remain beyond the energy range of the present experiment. In this respect there are significant similarities to superconducting $\text{Rb}_{0.89}\text{Fe}_{1.58}\text{Se}_2$ [11]. The sign reversal between effective intrablock (J_1) and interblock (J'_1) exchange interactions is clear evidence for the orbital degrees of freedom that underlie a wealth of exotic magnetic and electronic ground states in this class of

materials. The microscopic spin Hamiltonian that we can report for BaFe_2Se_3 will advance a quantitative understanding of short-range spin-orbital interactions in iron bearing square lattices and their potential role in promoting superconductivity.

The work at IQM was supported by the U.S. Department of Energy, Office of Basic Energy Sciences, Division of Material Sciences and Engineering, under Grant No. DE-FG02-08ER46544. This research at Oak Ridge National Laboratory's Spallation Neutron Source was sponsored by the U.S. Department of Energy, Office of Basic Energy Sciences, Scientific User Facilities Division. We are grateful to D. Abernathy for support on ARCS and to S. Tóth for making SPINW freely available.

*Present address: School of Physics, Georgia Institute of Technology, Atlanta, Georgia 30332, USA.
mourigal@gatech.edu

†Present address: Department of Chemistry, Colorado State University, Fort Collins, Colorado 80523, USA.

- [1] M. D. Lumsden and A. D. Christianson, *J. Phys. Condens. Matter* **22**, 203203 (2010).
- [2] P. Dai, J. Hu, and E. Dagotto, *Nat. Phys.* **8**, 709 (2012).
- [3] A. V. Chubukov, D. V. Efremov, and I. Eremin, *Phys. Rev. B* **78**, 134512 (2008).
- [4] C.-C. Lee, W.-G. Yin, and W. Ku, *Phys. Rev. Lett.* **103**, 267001 (2009).
- [5] R. M. Fernandes, A. V. Chubukov, J. Knolle, I. Eremin, and J. Schmalian, *Phys. Rev. B* **85**, 024534 (2012).
- [6] E. Dagotto, *Rev. Mod. Phys.* **85**, 849 (2013).
- [7] R. A. Ewings, T. G. Perring, R. I. Bewley, T. Guidi, M. J. Pitcher, D. R. Parker, S. J. Clarke, and A. T. Boothroyd, *Phys. Rev. B* **78**, 220501 (2008).
- [8] J. Zhao, D. T. Adroja, D.-X. Yao, R. Bewley, S. Li, X. F. Wang, G. Wu, X. H. Chen, J. Hu, and P. Dai, *Nat. Phys.* **5**, 555 (2009).
- [9] L. W. Harriger, H. Q. Luo, M. S. Liu, C. Frost, J. P. Hu, M. R. Norman, and P. Dai, *Phys. Rev. B* **84**, 054544 (2011).
- [10] O. J. Lipscombe, G. F. Chen, C. Fang, T. G. Perring, D. L. Abernathy, A. D. Christianson, T. Egami, N. Wang, J. Hu, and P. Dai, *Phys. Rev. Lett.* **106**, 057004 (2011).
- [11] M. Wang, C. Fang, D.-X. Yao, G. Tan, L. W. Harriger, Y. Song, T. Netherton, C. Zhang, M. Wang, M. B. Stone, W. Tian, J. Hu, and P. Dai, *Nat. Commun.* **2**, 580 (2011).
- [12] M. Liu, L. W. Harriger, H. Luo, M. Wang, R. A. Ewings, T. Guidi, H. Park, K. Haule, G. Kotliar, S. M. Hayden, and P. Dai, *Nat. Phys.* **8**, 376 (2012).
- [13] P. Abbamonte, G. Blumberg, A. Rusydi, A. Gozar, P. G. Evans, T. Siegrist, L. Venema, H. Eisaki, E. D. Isaacs, and G. A. Sawatzky, *Nature (London)* **431**, 1078 (2004).
- [14] B. Lake, A. M. Tselvik, S. Notbohm, D. Alan Tennant, T. G. Perring, M. Reehuis, C. Sekar, G. Krabbes, and B. Buchner, *Nat. Phys.* **6**, 50 (2010).
- [15] J. Schlappa, K. Wohlfeld, K. J. Zhou, M. Mourigal, M. W. Haverkort, V. N. Strocov, L. Hozoi, C. Monney, S. Nishimoto, S. Singh, A. Revcolevschi, J. S. Caux, L. Patthey, H. M. Ronnow, J. van den Brink, and T. Schmitt, *Nature (London)* **485**, 82 (2012).
- [16] J. M. Caron, J. R. Neilson, D. C. Miller, K. Arpino, A. Llobet, and T. M. McQueen, *Phys. Rev. B* **85**, 180405 (2012).
- [17] F. Du, K. Ohgushi, Y. Nambu, T. Kawakami, M. Avdeev, Y. Hirata, Y. Watanabe, T. J. Sato, and Y. Ueda, *Phys. Rev. B* **85**, 214436 (2012).
- [18] Z. V. Popović, M. Šćepanović, N. Lazarević, M. M. Radonjić, D. Tanasković, H. Lei, and C. Petrovic, *Phys. Rev. B* **89**, 014301 (2014).
- [19] X. Ke, B. Qian, H. Cao, J. Hu, G. C. Wang, and Z. Q. Mao, *Phys. Rev. B* **85**, 214404 (2012).
- [20] J. M. Caron, J. R. Neilson, D. C. Miller, A. Llobet, and T. M. McQueen, *Phys. Rev. B* **84**, 180409 (2011).
- [21] Y. Nambu, K. Ohgushi, S. Suzuki, F. Du, M. Avdeev, Y. Uwatoko, K. Munakata, H. Fukazawa, S. Chi, Y. Ueda, and T. J. Sato, *Phys. Rev. B* **85**, 064413 (2012).
- [22] B. Saparov, S. Calder, B. Sipos, H. Cao, S. Chi, D. J. Singh, A. D. Christianson, M. D. Lumsden, and A. S. Sefat, *Phys. Rev. B* **84**, 245132 (2011).
- [23] H. Lei, H. Ryu, A. I. Frenkel, and C. Petrovic, *Phys. Rev. B* **84**, 214511 (2011).
- [24] H. Lei, H. Ryu, V. Ivanovski, J. B. Warren, A. I. Frenkel, B. Cekic, W.-G. Yin, and C. Petrovic, *Phys. Rev. B* **86**, 195133 (2012).
- [25] C. Monney, A. Uldry, K. J. Zhou, A. Krzton-Maziopa, E. Pomjakushina, V. N. Strocov, B. Delley, and T. Schmitt, *Phys. Rev. B* **88**, 165103 (2013).
- [26] F. Ye, S. Chi, W. Bao, X. F. Wang, J. J. Ying, X. H. Chen, H. D. Wang, C. H. Dong, and M. Fang, *Phys. Rev. Lett.* **107**, 137003 (2011).
- [27] W.-G. Yin, C.-H. Lin, and W. Ku, *Phys. Rev. B* **86**, 081106 (2012).
- [28] Q. Luo, A. Nicholson, J. Rincón, S. Liang, J. Riera, G. Alvarez, L. Wang, W. Ku, G. D. Samolyuk, A. Moreo, and E. Dagotto, *Phys. Rev. B* **87**, 024404 (2013).
- [29] J. Rincón, A. Moreo, G. Alvarez, and E. Dagotto, *Phys. Rev. Lett.* **112**, 106405 (2014).
- [30] A. Georges, L. d. Medici, and J. Mravlje, *Annu. Rev. Condens. Matter Phys.* **4**, 137 (2013).
- [31] A. Krzton-Maziopa, E. Pomjakushina, V. Pomjakushin, D. Sheptyakov, D. Chernyshov, V. Svitlyk, and K. Conder, *J. Phys. Condens. Matter* **23**, 402201 (2011).
- [32] S. Dong, J.-M. Liu, and E. Dagotto, *Phys. Rev. Lett.* **113**, 187204 (2014).
- [33] M. B. Stone, J. L. Niedziela, D. L. Abernathy, L. DeBeer-Schmitt, G. Ehlers, O. Garlea, G. E. Granroth, M. Graves-Brook, A. I. Kolesnikov, A. Podlesnyak, and B. Winn, *Rev. Sci. Instrum.* **85**, 045113 (2014).
- [34] B. E. Warren, *Phys. Rev.* **59**, 693 (1941).
- [35] S. Nakatsuji, Y. Nambu, H. Tonomura, O. Sakai, S. Jonas, C. Broholm, H. Tsunetsugu, Y. Qiu, and Y. Maeno, *Science* **309**, 1697 (2005).
- [36] B. Dalla Piazza, M. Mourigal, M. Guarise, H. Berger, T. Schmitt, K. J. Zhou, M. Grioni, and H. M. Rønnow, *Phys. Rev. B* **85**, 100508 (2012).
- [37] S. Petit, *Collection SFN* **12**, 105 (2011).
- [38] S. Toth and B. Lake, *J. Phys. Condens. Matter* **27**, 166002 (2015).
- [39] A. C. Walters, T. G. Perring, J.-S. Caux, A. T. Savici, G. D. Gu, C.-C. Lee, W. Ku, and I. A. Zaliznyak, *Nat. Phys.* **5**, 867 (2009).